



AALBORG UNIVERSITY
DENMARK

Aalborg Universitet

Analysis of an interleaved control scheme employed in split source inverter based grid-tied photovoltaic systems

Nannam, Hari Charan; Banerjee, Atanu; Guerrero, Josep M.

Published in:
IET Renewable Power Generation

DOI (link to publication from Publisher):
[10.1049/rpg2.12108](https://doi.org/10.1049/rpg2.12108)

Creative Commons License
CC BY 4.0

Publication date:
2021

Document Version
Publisher's PDF, also known as Version of record

[Link to publication from Aalborg University](#)

Citation for published version (APA):
Nannam, H. C., Banerjee, A., & Guerrero, J. M. (2021). Analysis of an interleaved control scheme employed in split source inverter based grid-tied photovoltaic systems. *IET Renewable Power Generation*, 15(6), 1301-1314. <https://doi.org/10.1049/rpg2.12108>

General rights

Copyright and moral rights for the publications made accessible in the public portal are retained by the authors and/or other copyright owners and it is a condition of accessing publications that users recognise and abide by the legal requirements associated with these rights.

- Users may download and print one copy of any publication from the public portal for the purpose of private study or research.
- You may not further distribute the material or use it for any profit-making activity or commercial gain
- You may freely distribute the URL identifying the publication in the public portal -

Take down policy

If you believe that this document breaches copyright please contact us at vbn@aub.aau.dk providing details, and we will remove access to the work immediately and investigate your claim.

RPG 2022

Renewable Power Generation

22-23
September 2022


Meeting net
zero carbon

Savoy Place,
London

Call for papers deadline:
10 December 2021



Analysis of an interleaved control scheme employed in split source inverter based grid-tied photovoltaic systems

Hari Charan Nannam¹  | Atanu Banerjee¹ | Josep M. Guerrero²

¹ National Institute of Technology Meghalaya, Shillong Meghalaya, India

² Department of Energy Technology, Aalborg University, Aalborg East, Denmark

Correspondence

Hari Charan Nannam, National Institute of Technology Meghalaya, Shillong, Meghalaya, India.
Email: haricharan@nitm.ac.in

Funding information

Science and Engineering Research Board, Grant/Award Number: SB/S3/EECE/090/2016

Abstract

In conventional grid-tied renewable energy applications, the dc–dc converter is inevitable. An increased cost, size, and reduced efficiency are the demerits of incorporating a dc–dc converter. A recently introduced split source inverter (SSI) is capable to perform both dc–dc as well as dcac at a time. The main attractive controllable feature of SSI is its modulation index. By utilizing this parameter, an interleaved control structure is proposed for the SSI in grid-tied photovoltaic applications. The main objectives of the work are to track peak power and to maintain a stabilized voltage across the dc-link capacitor at a variable load and grid disturbances. The proposed peak power controller performs two important actions: (i) the peak power is traced at all irradiance and (ii) generates a duty cycle to enhance the dc-link capacitor voltage. The proposed scheme is essentially investigated with simulation. To validate experimentally, a 1 KW photovoltaic system is integrated into a grid-tied 10 kVA SSI prototype. A Xilinx based Spartan field-programmable gate array (FPGA) is used to provide a control algorithm for the SSI. Few case studies at different conditions are performed and investigated. Experimental and simulation results are presented to prove the robustness of the control strategy.

1 | INTRODUCTION

A conventional photovoltaic (PV) grid-tied system is a two-stage operation with a PV array, dc–dc converter, grid-tied dc–ac inverter. The standard voltage source/current source inverter (VSI/CSI) inevitably utilizes a dc–dc converter either to enhance (in VSI) or to diminish (in CSI) the input voltage [1]. Though a dc–dc converter stage is essential to extract peak power and magnify/lessen the input voltage, it suffers from certain drawbacks. In fuel cell applications, the dc–dc converter generates a high-frequency ripple current, and it is the primary reason for the decrease in fuel cell life span [1, 2]. To overcome the input or output current ripple due to the dc–dc converter, a filter (active/passive) may be implemented, but it results in increased cost and complexity of the system [2, 3]. Increased system size and reduced efficiency are also its demerits [1, 3]. To overcome these demerits, many single-stage converters that comprehend the dc/dc converter stage emerged out. The Z-source inverter [4] is regarded as the first application of the

impedance network in a single-stage family. In the later stages, many modified versions of the Z-source inverter are reported [1]. In the Z-source inverter, during the boost mode (shoot through), the load is short-circuited by any of the legs [4]. It results in a discontinuous input current and a high magnitude voltage across the x-shaped capacitors [5, 6]. To generate the shoot-through state, a supplementary switching state in addition to eight switching states is mandatory [5]. To overcome these demerits, three-phase and single-phase split source inverters (SSI) [5, 7, 8] were introduced. A detailed comparative analysis of different single-phase SSI is explained in the recent literature [7]. The benefits of the SSI are uninterrupted current input, similar pulse width modulation schemes which are implemented for conventional VSI, less passive component count, a continuous dc-link voltage [5, 9, 10]. In the literature [10], the author has chosen a step change in inductor current for an input current loop without any MPPT controller, and the dynamics of the PV source under transient conditions are not analyzed. The grid side analysis is performed in [10] by creating a voltage sag

This is an open access article under the terms of the [Creative Commons Attribution](https://creativecommons.org/licenses/by/4.0/) License, which permits use, distribution and reproduction in any medium, provided the original work is properly cited.

© 2021 The Authors. *IET Renewable Power Generation* published by John Wiley & Sons Ltd on behalf of The Institution of Engineering and Technology

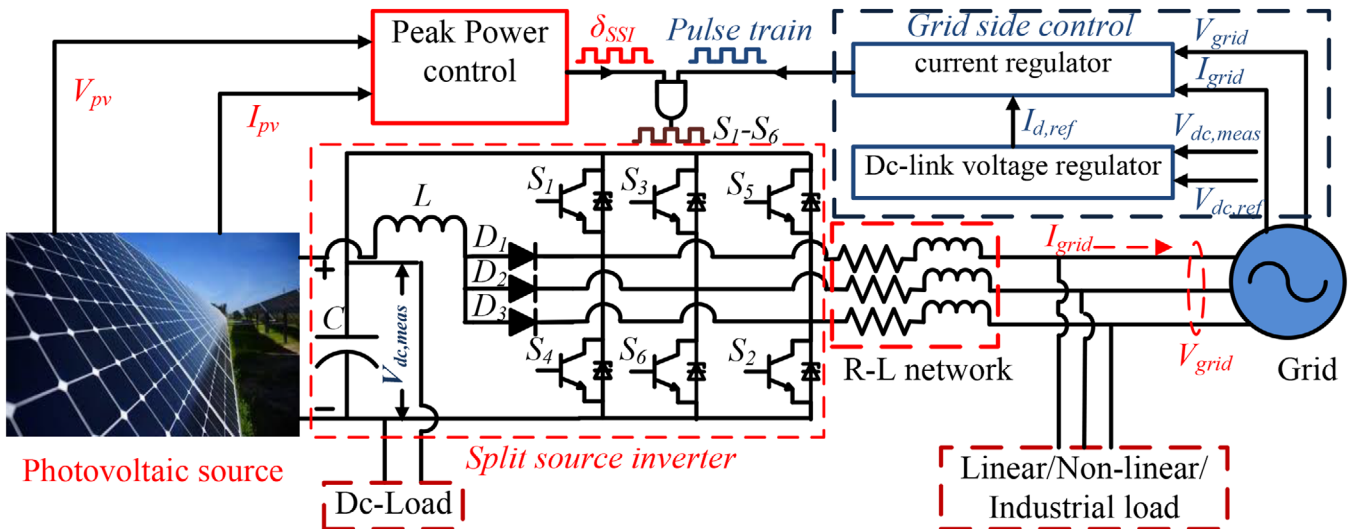


FIGURE 1 An SSI integrated PV grid-tied system with proposed control scheme

and swell of 15%. In addition to the aforementioned observation, the load analysis is performed on the ac and dc sides. The bioperational feature of SSI by adding a dc load across the dc-link capacitor is thoroughly examined in this concept. The main focus of the work is :

1. To design and evaluate the proposed peak power controller to track peak power from the PV system and produce a duty cycle for the SSI.
2. To investigate the steady-state analysis of SSI based grid-tied PV system.
3. To investigate the effects of variable irradiance on the proposed control scheme and the nature of SSI.
4. To study the effects of the load dynamics (both dc and ac) on the PV system and the proposed scheme.
5. To examine the effects of grid disturbance on the PV system as well as on the SSI.
6. Analysis of reverse operation of SSI is performed by connecting a local dc load across a dc-link capacitor and its effect on the PV system.

The entire PV grid-tied system, along with the proposed control scheme for SSI, is presented in Figure 1. The work consists of SSI's basic operational principle in Section 2, proposed control scheme in Section 3, discussion of results in Section 4, Section 5, the conclusion, and finally, the acknowledgment and references.

2 | BASIC PRINCIPLE OF OPERATION OF SSI AND PROPOSED CONTROL SCHEME

2.1 | Comparative analysis of different single-stage inverters

The comparative analysis is performed based on the switch and diode count, passive elements, switching states, the capability

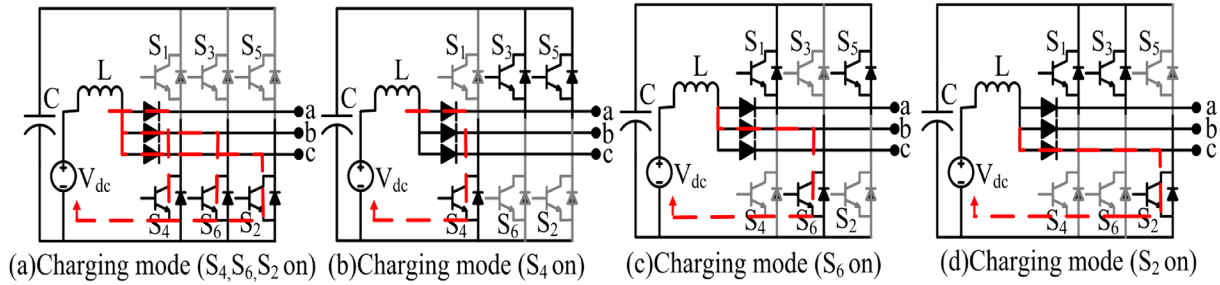
to boost, and the existence of the shoot through. The principal aim of SSI is to design a single-stage converter that works similarly to conventional VSI. From Table 1, ZSI [4] and Q-ZSI [11] consist of six switches with a diode and possess two capacitors and two inductors. Both the topologies inherit a shoot-through state to perform the boost operation. As a result, they consist of nine switching states. Later, CA-QZSI [12, 13], SL-QZSI [14], DA-QZSI [12, 13] were introduced. Though they inherit an improved performance of the ZSI, they consist of the higher passive component count. Later, an ASC-QZSI [12] was introduced to overcome the demerits of CA-QZSI [12, 13], SL-QZSI [14], DA-QZSI [12, 13]. Further improvements are noticed in CF-ZSI [15], where the shoot-through state is absent with a reduced diode count, but the passive component is more than the aforementioned topologies. SSI consists of six switches with three diodes, two passive elements, and the same switching states of conventional VSI. An increased efficiency, reduced converter size, low cost, and less complexity made the SSI more attractive in applying renewable energy systems. A detailed comparative analysis of different single-stage inverters is provided in Table 1.

2.2 | Operating principle of SSI

SSI is an amalgamation of impedance network with three diodes and a conventional VSI presented in Figure 1. The main features of SSI are [16]: stabilized dc-link voltage, continuous input current, the low voltage stress on semi-conductor switches, voltage boost capability, lesser passive component count, non-requirement of an additional switch as compared to conventional VSI, similar switching states and modulation scheme of VSI. The SSI also suffers from certain demerits like higher current stress on lower semi-conductor switches, higher voltage stress, and higher THD at lower voltage gains, commutation effect due to input diodes. The principle of operation can be explained based on charging and discharging modes of SSI.

TABLE 1 Comparative analysis of three-phase single-stage converters

Topology	Switches	Diodes	Passive components	Switching states	Boost	Shoot through
ZSI [4]	6	1	4	9	Yes	Yes
Q-ZSI [11]	6	1	4	9	Yes	Yes
SL-QZSI [14]	6	4	5	9	Yes	Yes
CA-QZSI [12, 13]	6	2	7	9	Yes	Yes
DA-QZSI [12, 13]	6	3	6	9	Yes	Yes
ASC-QZSI [12]	7	5	3	9	Yes	Yes
CF-ZSI [15]	6	1	5	6	Yes	No
SSI [5]	6	3	2	8	Yes	No

**FIGURE 2** The charging operation of SSI during the conduction of three lower switches and any one of the lower switch. (a) charging mode at S_6, S_4, S_2 are on (b) charging mode at S_6 are on (c) charging mode at S_4 are on (d) (b) charging mode at S_2 are on

1. Charging mode: The inductor (L) of the SSI is charged when any of the lower semi-conductor switches are turned-on. Among the eight switching states, six serve as active states, and two are zero states. All the six active states, including a zero state, facilitate the inductor's charging, as shown in Figures 2a–d and 3a–c.
2. Discharging mode: The energized inductor charges through the capacitor when all the upper semi-conductor switches are turned-on and when all the lower switches are turned-off, as shown in Figure 3d.

The average SSI voltage (V_{SSI}) in terms of input dc voltage (V_{dc}) is given as

$$V_{SSI} = \frac{4\pi}{2\pi - 3\sqrt{3}m} V_{dc}, \quad (1)$$

where m is the modulation index. In order to design an inductor and capacitor of SSI, low- and high-frequency components of current and voltage ripple should be considered, because they depend on duty cycle (δ_{SSI}) and switching frequency (f_{sw}).

$$\Delta I_{L,high} = (\delta_{SSI} V_{dc}) / (f_{sw} * L), \quad (2)$$

$$\Delta V_{C,high} = ((1 - \delta_{SSI}) * I_{dc}) / (f_{sw} * C). \quad (3)$$

On considering the fundamental quantities to model the low-frequency voltage and current ripple,

$$\Delta I_{L,low} = (m * V_{SSI}) / [(70 * \pi^2 * f_1 * L)], \quad (4)$$

$$\Delta V_{C,low} = (m * I_{dc}) / [(70 * \pi^2 * f_1 * C)]. \quad (5)$$

Finally, the C and L can be formulated as

$$L = [3\sqrt{3}(m * V_{SSI}) / (48 * \pi^2 * f_1 * (\Delta I_{L,high} + \Delta I_{L,low}))] + [\delta_{max}(V_{dc}) / 2(f_{sw} * (\Delta I_{L,high} + \Delta I_{L,low}))], \quad (6)$$

$$C = [3\sqrt{3}(m * I_{dc}) / (48 * \pi^2 * f_1 * (\Delta V_{C,high} + \Delta V_{C,low}))] + [1 - \delta_{min}(I_{dc}) / 2(f_{sw} * (\Delta V_{C,high} + \Delta V_{C,low}))]. \quad (7)$$

The detailed explanation of various modulation schemes of impedance network [17, 18] and the detailed explanation of SSI are presented in the literature [5, 17, 18].

2.3 | The proposed control scheme for SSI

This section discusses the proposed control scheme implemented in the SSI based PV grid-tied system. The reference paper [10] has given much importance to the grid-oriented control of SSI. Still, the effect of variable irradiance on tracking the peak power and its impact on the control system, the effects of load dynamics (both ac and dc), and grid disturbances on the PV system are not discussed. Here, a new control scheme is proposed to track the PV source's peak power. It also generates the corresponding duty cycle to enhance the dc-link voltage. In SSI, the duty cycle and the modulation index are equal to each other and need to be interleaved to control independently.

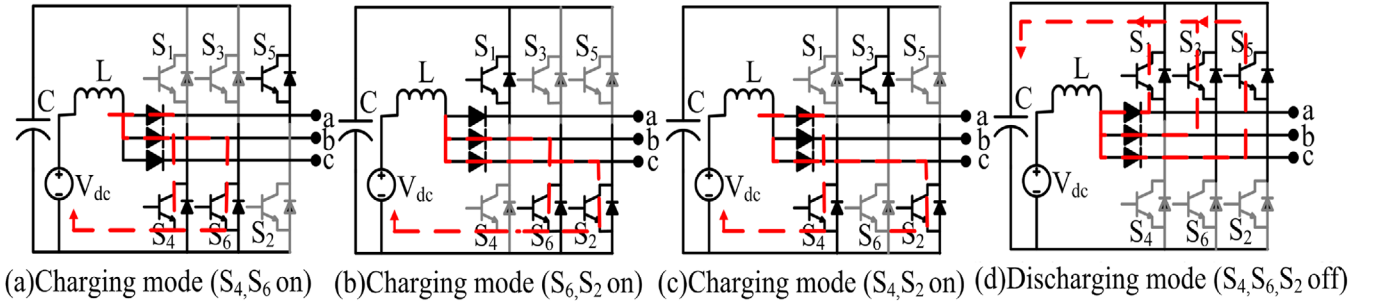


FIGURE 3 The charging operation of SSI during the conduction of any two lower switches and the discharging operation at the conduction of three upper switch. (a) charging mode at S_6, S_4 are on (b) charging mode at S_6, S_2 are on (c) charging mode at S_4, S_2 are on (d) Discharging mode at S_4, S_6, S_2 are off

The SSI inherently generates a duty cycle to enhance the dc-link voltage. In renewable energy system applications, the duty cycle has to be generated by a peak power controller to facilitate the maximum power transfer. In this paper, the duty cycle of SSI is produced by an external controller to enhance the voltage and track the peak power. The proposed scheme embraces the same synchronous reference frame used in conventional grid-connected VSI. The grid-oriented control comprises a regulator for dc-link voltage at variable irradiance, variable loads and grid side disturbances, and a current regulator loop to control the inverter output currents. In a renewable energy application, peak power tracking is one of the essential criteria to be considered. So, a peak power control is also presented to track the peak power. The detailed analysis of each control loop existed in grid-oriented control, and MPPT control is elucidated in subsequent sections.

2.3.1 | Peak power control

The modulation index (m) and duty cycle (δ_{SSI}) of SSI are related to each other. The inductor (L) is charged when the modulation index (m) is equal to duty cycle (δ_{SSI}) [5, 10]. The important relations between δ_{SSI} and m are expressed as [5]:

$$\delta_{SSI}(\Theta) = 0.5 - (0.5m) * \sin(\Theta), \quad (8)$$

where $(7\pi/6) \leq (\Theta) \leq (11\pi/6)$, The upper and lower limits of δ_{SSI} are

$$\delta_{SSI,max} = 0.5 + 0.5m, \quad (9)$$

$$\delta_{SSI,min} = 0.5 - 0.25m. \quad (10)$$

The $\delta_{SSI,ave}$ for an inductor to charge is given as

$$\delta_{ave} = 0.5 + (1.299m/\pi). \quad (11)$$

The main aim of the proposed peak power controller is to track the peak power and to produce a duty cycle (δ_{pv}) equal to the modulation index (m). The control scheme of the peak power controller is presented in Figure 4. In this proposed scheme,

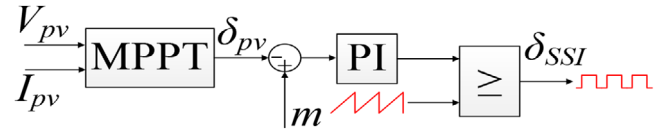


FIGURE 4 The proposed peak power controller

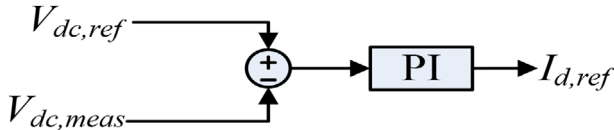
the perturb and observe algorithm [19, 20] is chosen to track the peak power from corresponding solar radiation. The voltage and current of the PV system are the inputs for the MPPT algorithm. It calculates the power generated by the PV source equivalent to the PV voltage and current. A duty cycle is generated according to the power variations [20]. The source duty cycle (δ_{pv}) is programmed to operate in between the upper and lower values of the SSI duty cycle, so that the optimum performance of SSI may be guaranteed. The duty cycle (δ_{pv}) is compared with the modulation index (m) of SSI. The error $\Delta\delta$ which is obtained by comparing the modulation index and δ_{pv} is fed to a well-tuned PI controller. Table 2 consist of the values $K_{p\delta}$ and $K_{i\delta}$. The signal generated by the PI controller is collated with a triangular wave to produce a duty cycle for SSI (δ_{SSI}). Hence, the proposed scheme not only generates a duty cycle for the SSI but also tracks the peak power. A logical AND gate is implemented to merge δ_{SSI} and m . The parameters of the PI regulator are chosen lower than the dc-link voltage controller to provide sustainable performance.

2.3.2 | DC-link voltage regulator

The intermittent nature of irradiance generates a variable power, which develops transients on the dc-link voltage. A sudden increase/decrease in irradiance either increases or decreases the generated power. As a result, an overshoot/undershoot is experienced on the dc-link voltage, which means the dc-link voltage stability is lost. So, the predominance of dc-link voltage is associated with the power feeding to the grid. A change in the reference current of the current control loop generated by the dc-link regulator is the consequence of feeding an increased power or a lessened power from the PV source. The dc-link voltage control scheme is presented in Figure 5. The dc-link voltage undergoes variations when (a) power exchanged by the dc-link varies

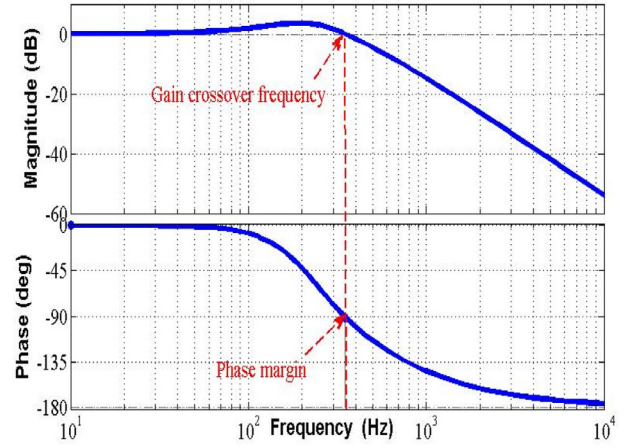
TABLE 2 System specifications for simulation

PV system (Mitsubishi PV-UD190)	Values
Open circuit voltage V_{oc} (V)	30.8006
Short circuit current I_{sc} (A)	8.2329
Voltage at MPP V_{mpp} (V)	24.699
Current at MPP I_{mpp} (A)	7.7127
$\alpha_{V_{oc}}$	-0.105
$\alpha_{I_{sc}}$	0.004446
No. of series connected modules in a string	6
No. of parallel strings	1
Irradiance (W/m^2)	1000, 800, 600
Temperature (degree Celsius)	25
SSI	Values
Dc-link capacitance (μF)	177.3
Input inductance (mH)	1.68
Dc voltage regulator	Values
K_p	0.7
K_f	8
$V_{dc,ref}$ (V)	1000
Current regulator regulator	Values
K_p	0.05
K_f	0.02
Maximum power control regulator	Values
$K_{p\delta}$	-0.005
$K_{f\delta}$	-0.02
Grid parameters	Values
r_g (m Ω)	0.8
L_g (mH)	5.8

**FIGURE 5** The control structure of dc-link voltage regulator and the generation of $I_{d,ref}$

(also includes when there is a sudden change in the load connected at the dc-link point [dc load] or the grid [three-phase load]), (b) the grid experiences an unbalance [21, 22], and (c) at variable solar radiation. In dc-link voltage regulator, the dc-link voltage reference, $V_{dc,ref}$ is compared with measured dc-link voltage ($V_{dc,meas}$). If the difference in the dc-link voltage exists, it implicates the loss in energy at the dc-link. So, the dc-link voltage should revert to the recommended voltage to transfer the maximum power. The recommended or reference value of the dc-link voltage regulator is given as [23, 24] :

$$V_{dc,ref} \geq \frac{2 * V_{abc,SSI}}{\sqrt{6} * m_{abc}}, \quad (12)$$

Bode diagram for dc-link voltage regulator in closed loop**FIGURE 6** A Bode plot representation of dc-link voltage regulator loop

where $V_{abc,SSI}$ is the rms voltage of SSI and m_{abc} is the modulation index of SSI.

The instantaneous power balance equation in a synchronously rotating dq reference frame under the assumption of loss less condition can be expressed as [25],

$$\frac{3}{2} [V_{gd}i_d + V_{gq}i_q] = V_{dc}i_0 - V_{dc}C \frac{dV_{dc}}{dt}, \quad (13)$$

V_{gd}, V_{gq}, i_d, i_q are the dq components of three-phase voltage and current parameters of grid, i_0 is the output current of the PV cell.

The transfer function \hat{v}_{dc}/\hat{v}_d can be represented as:

$$\begin{aligned} G_{dc-link} &= \frac{\hat{v}_{dc}}{\hat{v}_d} \\ &= \frac{3V_{gd}}{2(i_0 - V_{dc}CS)}. \end{aligned} \quad (14)$$

The transfer function of dc-link voltage under disturbed grid condition, $\hat{v}_{dc}/\hat{v}_{gd}$ is represented as:

$$\frac{\hat{v}_{dc}}{\hat{V}_{gd}} = \frac{\sqrt{3}}{1 - \frac{V_{dc}CS}{i_0}}. \quad (15)$$

The values for K_p and K_f , $V_{dc,ref}$ for dc-link voltage regulator are provided in Table 2. The values of PI for dc-link voltage regulator are computed using symmetrical optimum procedure [26]. The Bode plot representation of dc-link voltage controller is presented in Figure 6. The closed loop gain crossover frequency of the voltage controller is 350 Hz and the phase margin is 90° . The calculated bandwidth is 56 Hz.

2.3.3 | Current controller

The main aim of the current controller is to modulate the grid side current, to provide protection, and to handle the issues of

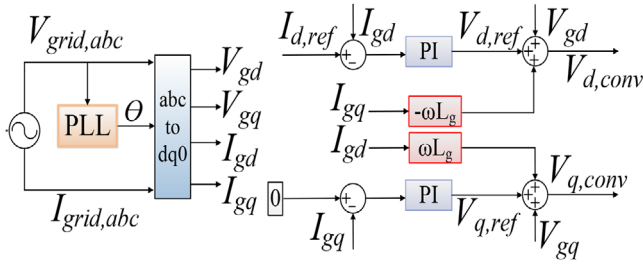


FIGURE 7 The control structure of current control loop

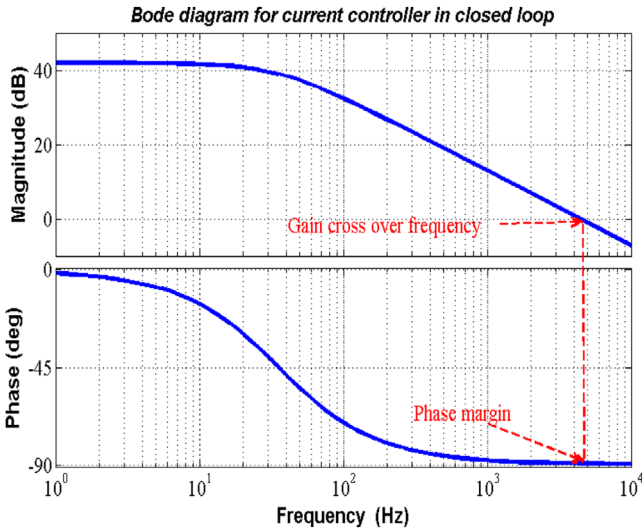


FIGURE 8 The Bode plot representation of current control loop

power quality [27]. The control structure of the current controller is presented in Figure 7. The motive of the paper is to regulate the real power feeding to the grid, so $i_{d,ref}$ and $i_{q,ref}$ (zero) are considered. V_{gd} , V_{gq} , I_{gd} , I_{gq} are generated from the grid voltage and grid currents as shown in Figure 7. The equations governing the current controller can be described as [28]:

$$V_{d,conv} = V_{gd} + r_g i_{d,ref} - \omega i_{q,ref} + L_g \frac{di_{d,ref}}{dt}, \quad (16)$$

$$V_{q,conv} = V_{gq} + r_g i_{q,ref} + \omega i_{d,ref} + L_g \frac{di_{q,ref}}{dt}, \quad (17)$$

where L_g , r_g are the grid side filter and internal resistance, ω is the grid angular frequency. The current controller transfer function in closed loop is represented as:

$$G_{cc} = \frac{1}{s\tau_i + 1}, \quad (18)$$

where τ_i is the time constant of closed loop current regulator and can be selected below 5 ms for better utilization [29]. The Bode analysis for the current regulator in closed loop is presented in Figure 6. The gain crossover frequency of current controller in closed loop is presented in Figure 8 and is computed as

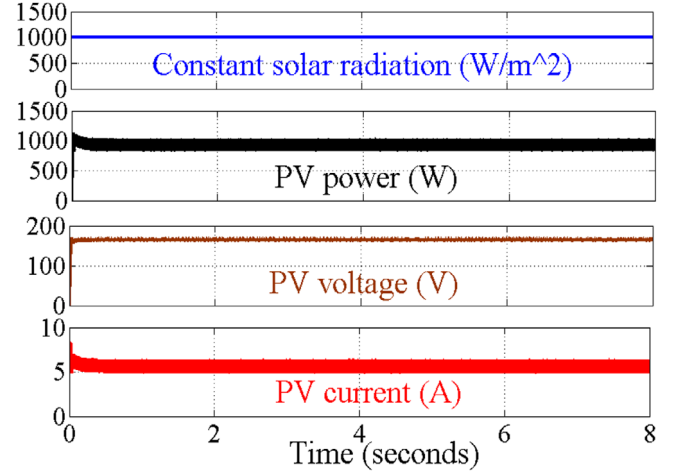


FIGURE 9 Constant irradiance (W/m^2), output power of PV, PV terminal voltage, PV output current

4500 HZ and the phase margin is 90° . The bandwidth calculated according to [28] is found to be 716 Hz.

3 | DISCUSSION OF THE SIMULATION AND EXPERIMENTAL RESULTS

3.1 | Simulation results

The entire system with the proposed control scheme is primarily assessed in MATLAB/SIMULINK. A Mitsubishi PV-UD190 is used as a PV system for simulation. Each parameter used in the simulation is listed in Table 2. Different cases are selected and analyzed to observe the optimum performance of the proposed control scheme. The proposed control scheme's objectives, which are mentioned in Section 1, are evaluated using different test cases.

3.1.1 | Case-I: Steady-state analysis (constant solar radiation and without load)

In case-I, constant solar radiation without the load is considered. As the irradiance is stable, the PV voltage and current remain unchanged, as shown in Figure 9. As there is no change in solar radiation, PV voltage is constant. As a result, dc-link voltage, SSI output voltage, and currents remained constant. The peak power controller tracks the maximum power from the PV source and is presented as PV power in Figure 9. The dc-link voltage, the voltage, and currents of SSI are shown in Figure 10.

3.1.2 | Case-II: Variable irradiance and without load

In this case, a change in solar radiation and its impact on the proposed control scheme is investigated. Three different solar radiations 1000, 800, 600 W/m^2 at different time instants are

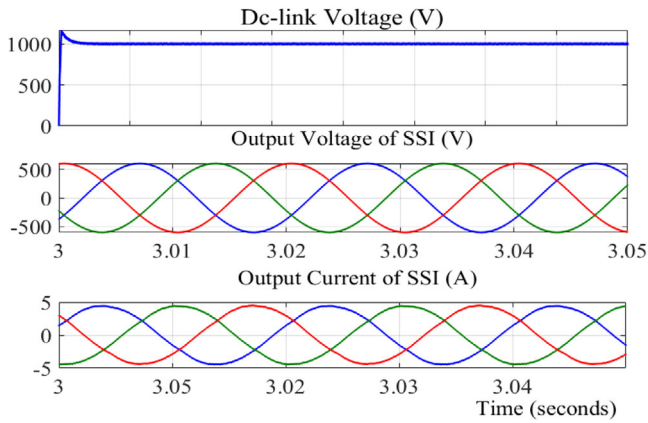


FIGURE 10 Steady-state analysis of dc-link voltage, terminal voltage, and currents of SSI

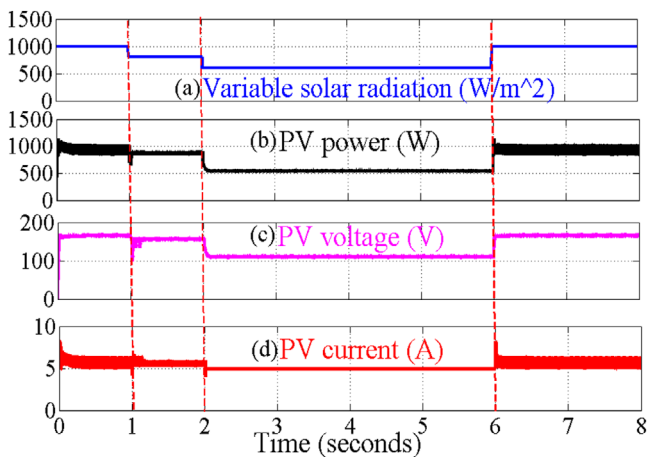


FIGURE 11 (a) Variable irradiance (W/m^2). (b) Output power of PV. (c) PV terminal voltage. (d) PV output current

considered. At time $t = 1$ s, the irradiance is changed from 1000 to 800 W/m^2 , at $t = 2$ s, the irradiance is changed from 800 to 600 W/m^2 , and finally, the irradiance is increased from 600 to 1000 W/m^2 as shown in Figure 11. According to the change in irradiance, PV voltage, PV current, and power generated by PV experience a change. The solar radiation, PV voltage, PV current, and PV power are presented in Figure 11. The effect of irradiance on the dc-link voltage at different irradiance is shown in Figure 12. Since the dc-link capacitor is directly associated with the PV system, the impact of atmospheric changes will reflect directly on the dc-link voltage. The dc-link voltage is maintained constant, as a result, the filtered output voltage of SSI also remained constant as shown in Figure 13. The change in SSI screened current at different irradiance is presented in Figure 13a–c.

3.1.3 | Case-III: Variable irradiance and variable dc load

In case-III, a variable dc load is connected across the dc-link capacitor under the consideration of variable irradiance. The

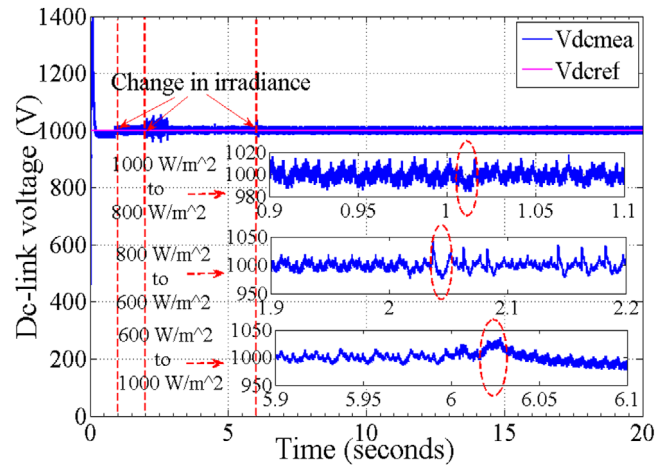


FIGURE 12 The effect of variable solar radiation on dc-link voltage

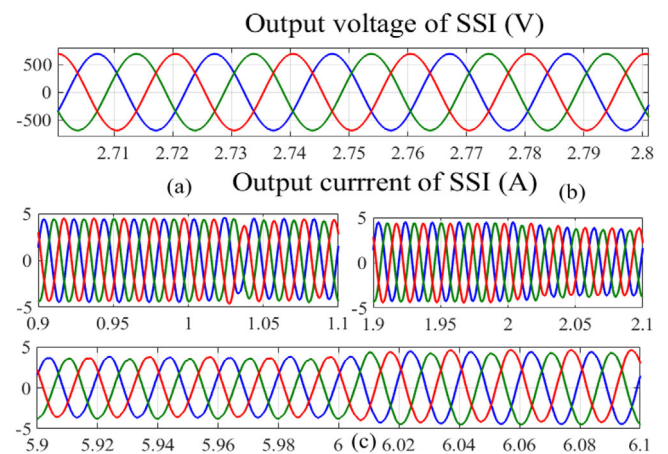


FIGURE 13 SSI output voltage and current under variable solar radiation at time (a) $t = 1$ sec, (b) $t = 2$ sec, and (c) $t = 6$ sec.

irradiance is made to change at $t = 1$ s, $t = 2$ s, $t = 6$ s, as shown in Figure 14. The series and shunt resistances used in this paper are 1011.1501 and 0.2231 Ω . The constraint for the PV source to operate as a constant current source is [30]:

$$R_{in} = \left(\frac{I_d}{V} + \frac{1}{R_p} \right) + R_s > \frac{V}{I}. \quad (19)$$

The calculated value of R_{in} is greater than the calculated value of $\frac{V}{I}$, so the PV source is operating as a constant current source which is shown in Figure 14. The effect of two different dc loads on dc-link voltage and the power consumption is shown in Figures 15 and 16. At $t = 3$ s, a load of 500 W is turned-on, and at $t = 5$ s, a load of 100 W is turned-on, which is represented in Figures 15a and 16a. The power consumption of the 500 W load and the current flowing into the load are presented in Figure 15d and Figure 15c, respectively. Similarly, a load of 100 W is turned-on at $t = 5$ s, which is presented in Figure 16a. The voltage dip for a moment, the current flowing into the load, and power consumed by the 100 W load are presented in Figure 16b–d. The combined effect of variable irradiance and sudden step change

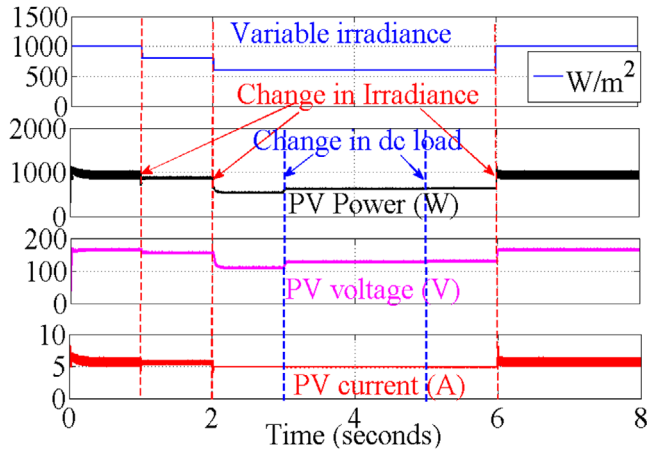


FIGURE 14 The effect of variable dc load on PV voltage, current, and power

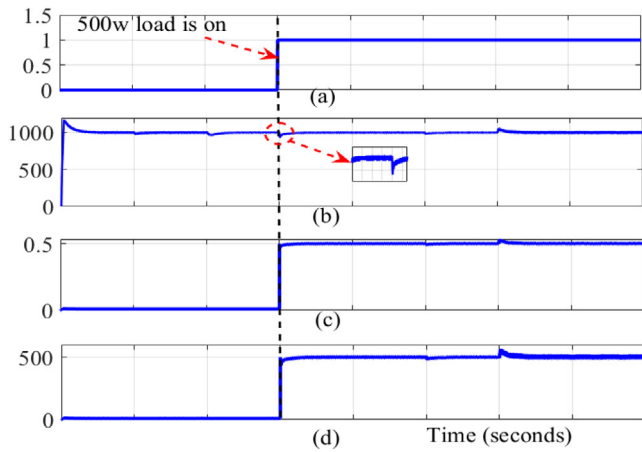


FIGURE 15 (a) Load switching instants. (b) Transient in dc-link voltage when 500W load is turned-on. (c) Magnitude of current at 500 W load. (d) Power consumed by the load

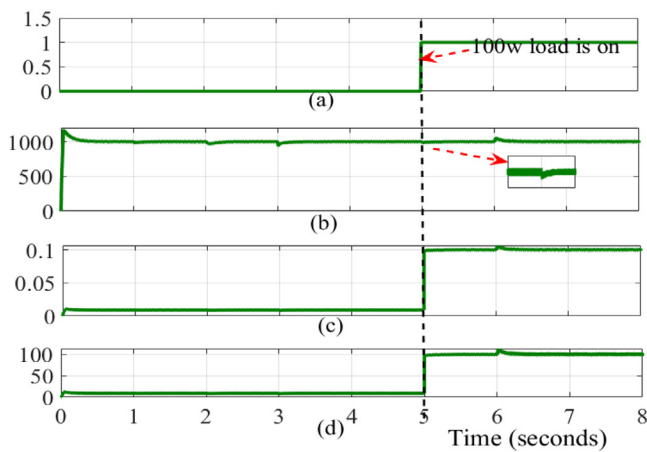


FIGURE 16 (a) Load switching instants. (b) Transient in dc-link voltage when 100 W load is turned-on. (c) Magnitude of current to 100 W load. (d) Power consumed by 100 W load

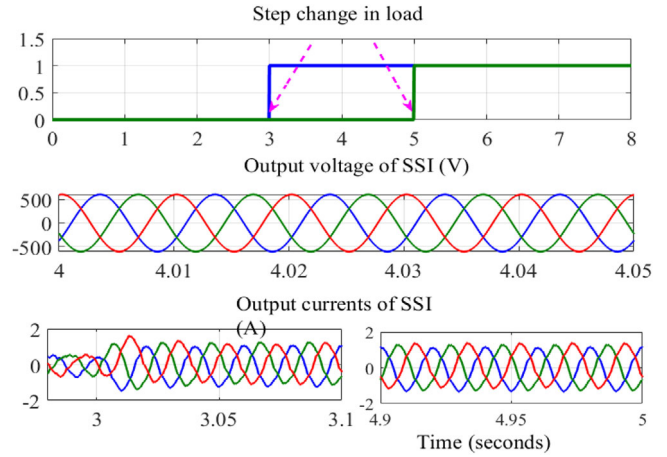


FIGURE 17 The combined effect of variable irradiance and step change in dc load and their effect on SSI voltage and currents

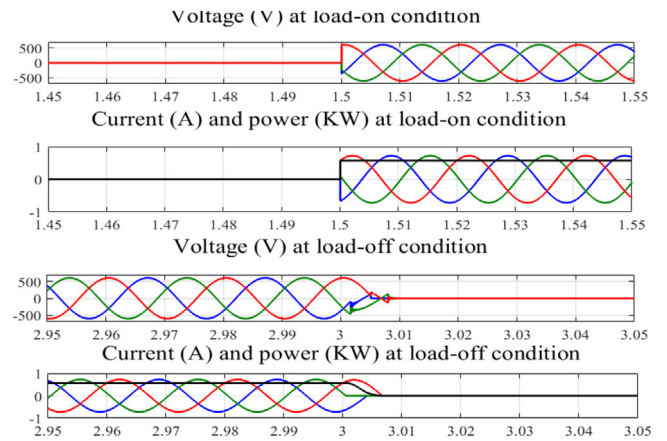


FIGURE 18 The three-phase voltage, current, and power (represented by black colour) consumed by three-phase load

in a load along with SSI voltage and currents are presented in Figure 17.

3.1.4 | Case-IV: Variable irradiance and variable three-phase ac load connected to the grid

In this case, a three-phase load of 400 W is connected to the grid. The load is switched-on at $t = 1.5$ s, $t = 4.5$ s, and turned-off at $t = 3$ s, $t = 5$ s. A three-phase voltage across the load, load current, and power consumed by the load on and off positions is presented in Figure 18. When the load is turned-on at $t = 1.5$ s, the dc-link voltage undergoes a voltage dip and later regains to the reference value. The grid starts to supply power to the load at this instant due to PV power's insufficiency. As a result, the grid current magnitude is raised to some extent and later attained its natural position when the load is turned-off, as shown in Figure 19.

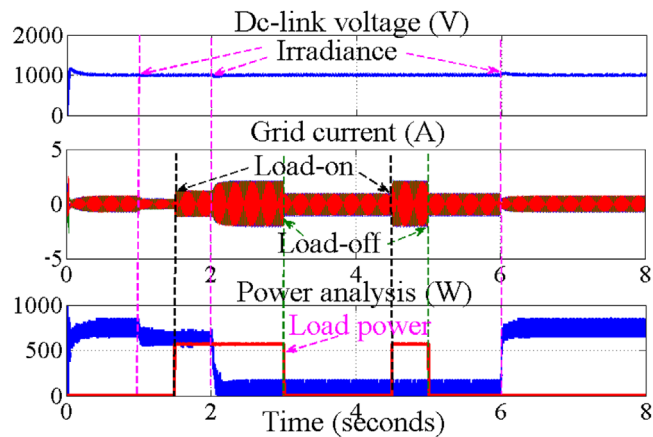


FIGURE 19 The effect of three-phase ac load connected on dc-link voltage and output current of SSI and the analysis of power

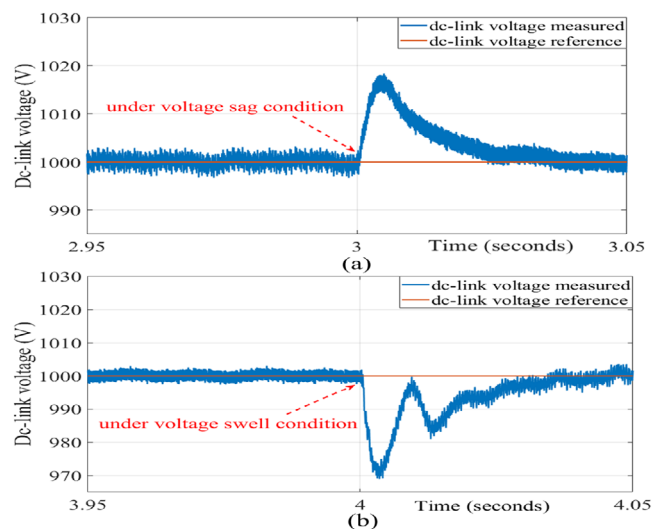


FIGURE 20 The effect of (a) voltage sag and (b) swell on dc-link voltage

3.1.5 | Case-V: Variable irradiance with voltage sag and swell condition

In this case, the effect of grid disturbances along with the change in irradiance is considered. The irradiance changes at time $t = 1, 2$ s, and $t = 6$ s. At this time, the SSI's sinusoidal voltage remains constant due to the constant voltage generated by the dc-link voltage controller. The magnitude of SSI output current changes according to the change in irradiance. The voltage sag of 20% is created at a time, $t = 3$ s, and voltage swell of 20% is created at a time $t = 4$ s, in this work. The effect of grid side disturbance on dc-link voltage is presented in Figure 20. The output current of SSI at variable irradiance and grid side disturbances is presented in Figure 21. The dc-link voltage experiences voltage overshoot during the voltage sag and retains its initial position due to a robust dc-link voltage controller, as shown in Figure 20a. During the voltage swell, the dc-link voltage experiences voltage undershoot and returns to the initial, as presented in Figure 20b. The dc-link voltage

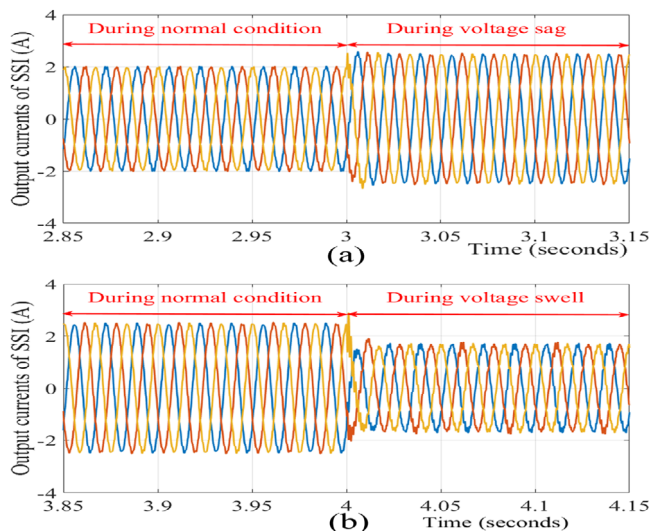


FIGURE 21 The effect of voltage sag and swell on the output current of SSI (a) Effect of voltage sag (b) effect of voltage swell

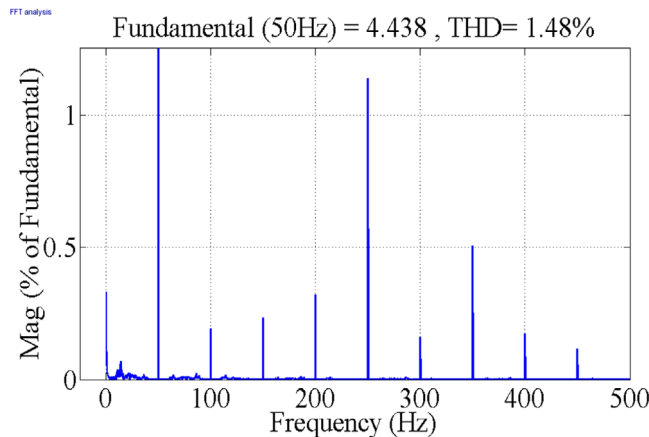


FIGURE 22 FFT analysis of the currents injected into the grid

regulator generates $I_{d, ref}$, which commands the current controller. According to the current controller's command, the current's magnitude is increased during the voltage sag, as shown in Figure 21a. Similarly, the current magnitude is reduced during the voltage swell, as shown in Figure 21b. The FFT analysis of the currents injected into the grid is presented in Figure 22.

3.2 | Experimental analysis

An experimental prototype with all necessary auxiliary equipment used in this paper is presented in Figure 23. A PV array of four panels, which is approved by Ministry of New and Renewable Energy (MNRE), is used to generate a power of 1 KW, in which each panel can generate 250 W. A self-powered SP-110 pyranometer designed by Apogee Instruments, USA, is used to sense the variable solar radiation. The maximum calibrated output range is 400 mV. To convert the sensor signal to short wave radiation ($\frac{W}{m^2}$), multiply the sensor signal (mV) with calibration

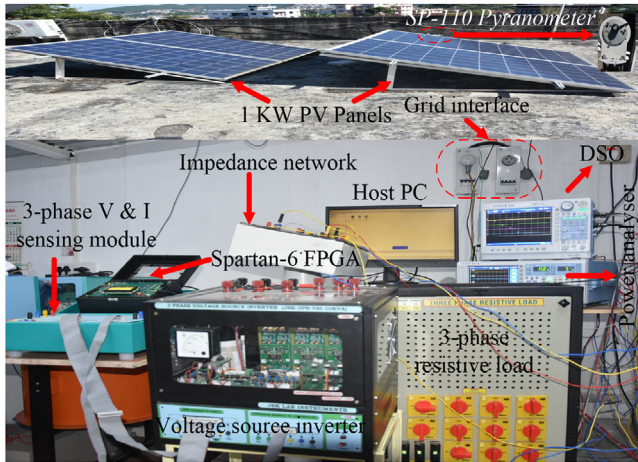


FIGURE 23 An experimental setup to analyze the system in real-time environment

factor $\left(\frac{W}{m^2}\right)$. A 5 mH, 10 A inductor, 450 V, 330 μ F capacitor are used to provide an impedance network for the VSI, and three MUR30120PTG ultrafast recovery diodes are used in the impedance network board as shown in Figure 23.

A three-phase VSI, which is made up of three SKM100GB12T4 IGBTs, is used in this prototype. A three-phase voltage, current from the grid, and the load are sensed by LV20-P and HE055T01 sensors and fed back to the controller using operational amplifier T1082 and AD7366 analog to digital converter (ADC). The measured voltage across the capacitor and the grid voltage and currents are feedback to the Spartan-6 XC6SLX25 field-programmable gate array (FPGA) to generate controlled pulses to semikron IGBTs by sinusoidal pulse width modulation (SPWM). A three-phase resistive load is used to perform the load analysis. A three-phase variable autotransformer is used at the grid to generate voltage sag and swell. Yokogawa WT 1800 precision power analyzer, DL850E Yokogawa scope corder, and keysight DSOX2014A digital storage oscilloscope are used to analyze the real-time results. The analysis of grid-tied SSI under constant solar radiation is investigated in Figure 24. The PV voltage (V_1) and current (I_1) are constant due to the aforementioned condition. As PV Voltage generated by the PV panel is constant, the dc-link voltage (V_2) also remains constant. The two-level SSI voltage (V_3) and current (I_3) under constant irradiance condition is presented in Figure 24. Since no load is connected either across dc terminals or at the ac side, the grid voltage (V_4) and current (I_4) remained transient free, and the total power generated by the PV system is fed to the grid. The analysis of variable solar irradiation on the SSI control scheme is investigated, and the outcome is presented in Figure 25. A sudden decrease in solar radiation results in a sudden change in PV current (CH2), as shown in Figure 25. As a result, the dc-link voltage (CH3) experiences a voltage undershoot and returns to the reference value due to a well-tuned PI controller. The grid voltage (CH5) remained constant, but the grid current (CH6) experienced

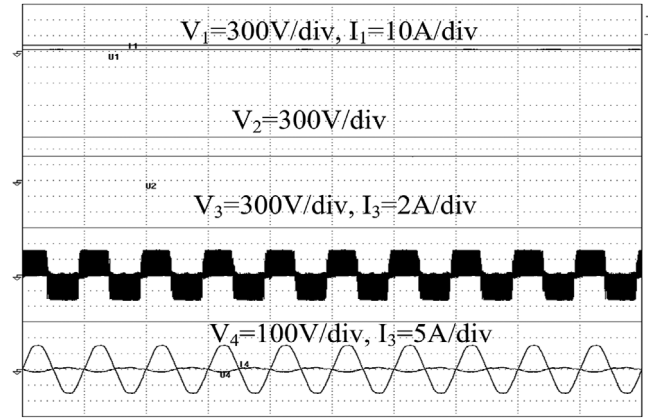


FIGURE 24 The dc-link voltage (V_2), two level voltage (V_3) and current (I_3), grid voltage (V_4) and current (I_4) at constant PV voltage (V_1) and current (I_1) for case-I as mentioned in Section 3

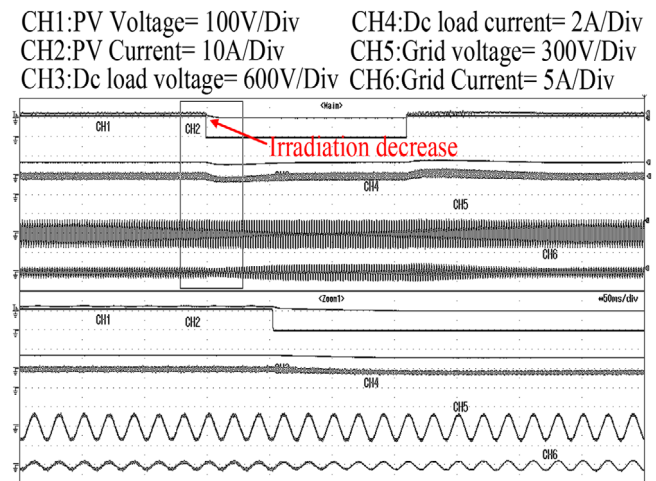


FIGURE 25 The effect of variable irradiance on the dc-link voltage regulator and current controller for case-I and case-II as mentioned in Section 3

a decreased magnitude. The zoomed version of the transient analysis is also presented in Figure 25. The rectangular section of Figure 25 is zoomed-in and presented below to have a clear understanding at the time of transient. The PV voltage and current sensed by SP-110 at different solar radiations are presented in Figure 26. The peak power tracked by the MPPT controller at different solar radiations is also recorded in Figure 26. In the conquest of exploring the bidirectional operation of SSI, a dc load is connected across the dc-link capacitor. The dc load received power from the grid at low irradiance and from the PV source at higher irradiance. A transient analysis is performed on the SSI based PV grid-tied system by a sudden change in the dc load. A dc load is suddenly turned-on; as a result, the PV voltage (CH1) experiences a voltage dip, and the PV current (CH2) abruptly increases as in Figure 27a. The dc-link voltage regulator stabilizes the dc-link voltage (CH3) even after the voltage overshoot. The effect of the sudden increase of dc-load on the grid current (CH6) is presented in Figure 27a.

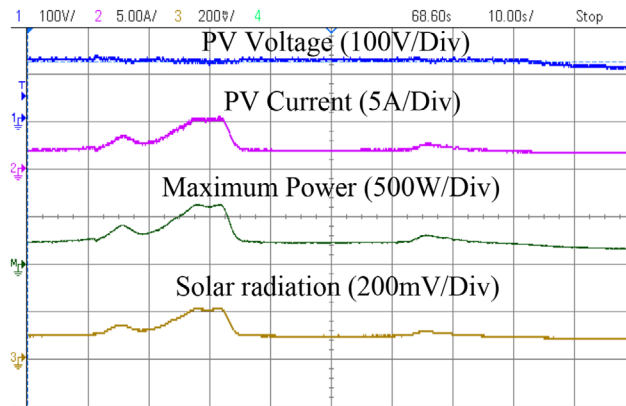
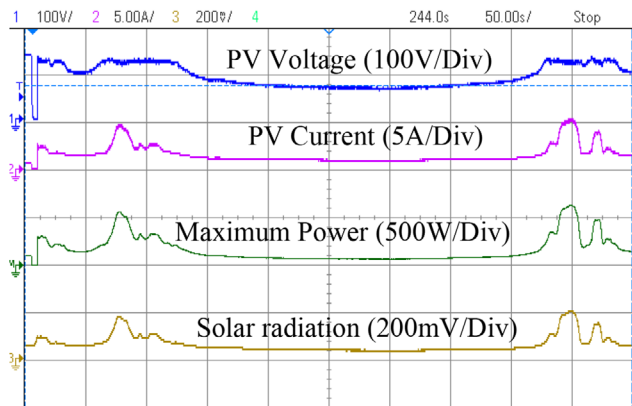
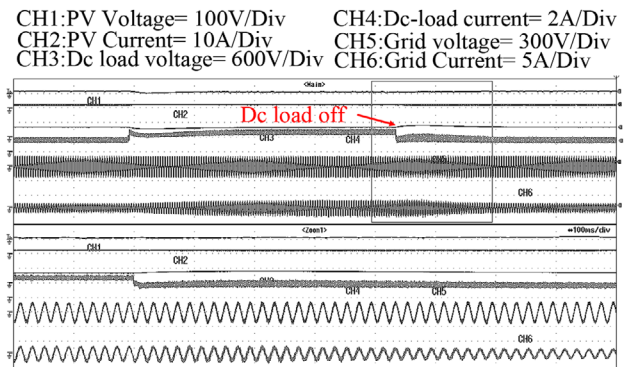
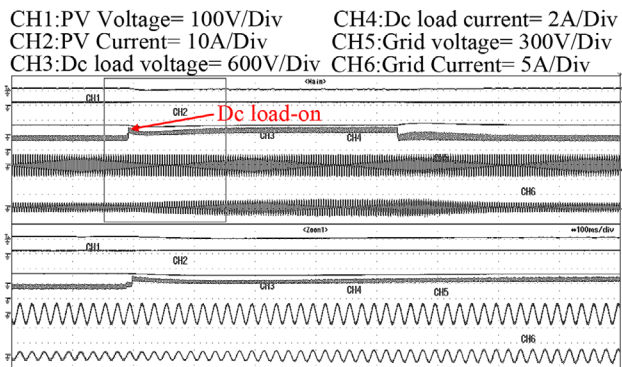


FIGURE 26 The PV voltage (blue colour), PV current (pink colour), maximum power (green colour) at different irradiance (yellow colour) sensed by SP-110



(a) The effect of sudden turn-on of dc load on SSI based PV grid-tied system

(b) The effect of sudden turn-off of dc load on SSI based PV grid-tied system

FIGURE 27 The effect of sudden change in dc load on PV system and grid as mentioned in test case-III of section-3 (a) The effect of sudden turn-on of dc load on SSI based PV grid-tied system (b) The effect of sudden turn-off of dc load on SSI based PV grid-tied system

Similarly, the effect of a sudden decrease of dc load is presented in Figure 27b. The zoomed version of the above-mentioned changes is presented in Figure 27a ,b itself. The effect of a three-phase load on the designed controller and PV grid-tied system is presented in Figure 28. The sudden increase in the three-phase ac load increases the PV current (CH2), as shown in Figure 28a. The dc-link voltage regulator controls the dc-link voltage (CH3); as a result, the PV current (CH2) restores to its original state as in Figure 28a. A similar analysis is implemented for a sudden decrease in ac load, and the results are presented in Figure 28b. The effect of voltage sag and swell on the SSI based PV grid-tied system is shown in Figure 29. A sudden change in the grid voltage (CH4) perturbs the PV voltage (CH1). The voltage regulator mitigates the transients in the dc-link voltage (CH3). To compensate for the voltage sag, the grid currents (CH6) increases in magnitude to maintain constant power flow, as shown in Figure 29a. For a clear understanding, the zoomed version of the voltage sag phenomena is shown in Figure 29a. The effect of voltage swell on the PV system with its zoomed version is presented in Figure 29b. The FFT analysis of grid voltage and current in real time is presented in Figure 30. The

FFT analysis of the grid voltage and currents are calculated using the formula mentioned in the literature [31]:

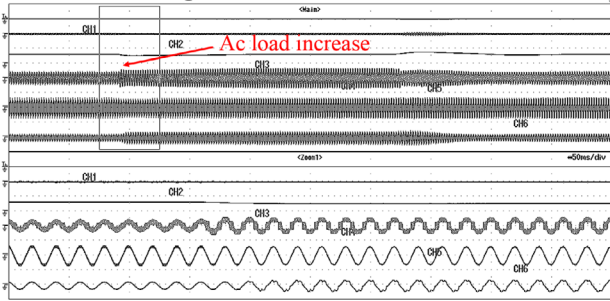
$$V_{THD} = \frac{\sqrt{\sum_{n=2}^{\infty} V_{n,RMS}^2}}{V_{1,RMS}}, \quad (20)$$

$$I_{THD} = \frac{\sqrt{\sum_{n=2}^{\infty} I_{n,RMS}^2}}{I_{1,RMS}}, \quad (21)$$

where $V_{1,RMS}$ and $I_{1,RMS}$ are the fundamental frequency signals of the voltage and current, $V_{n,RMS}$ and $I_{n,RMS}$ are the square root summation of all the frequencies other than the fundamental ($n = 2, 3, \dots, \infty$).

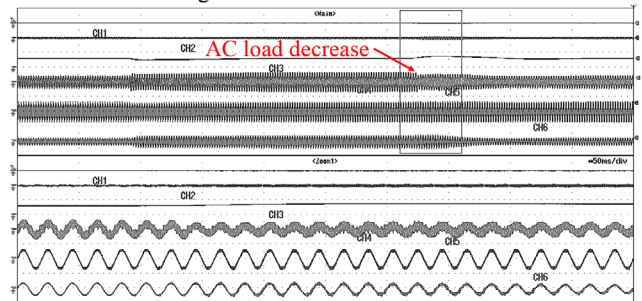
The THD values of grid voltage and current are found to be 2.763 and 2.993 from the numerical data presented in Figure 30, which are less than the standard values of THD, according to IEEE 519-2014 [32]. The efficiency is usually calculated as the ratio of the input power and losses with input power or the output power to the input power [31]. The system's efficiency at

CH1:PV Voltage= 100V/Div CH4:AC load current= 2A/Div
 CH2:PV Current= 10A/Div CH5:Grid voltage= 300V/Div
 CH3:Dc-link voltage= 600V/Div CH6:Grid Current= 5A/Div



(a) The effect of sudden increase of three-phase ac load on SSI based PV grid-tied system

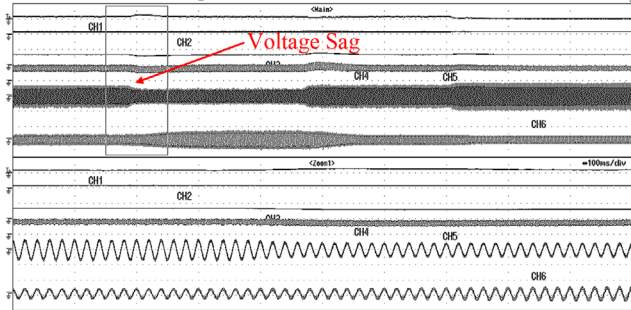
CH1:PV Voltage= 100V/Div CH4:AC load current= 2A/Div
 CH2:PV Current= 10A/Div CH5:Grid voltage= 300V/Div
 CH3:Dc-link voltage= 600V/Div CH6:Grid Current= 5A/Div



(b) The effect of sudden decrease of three-phase ac load on SSI based PV grid-tied system

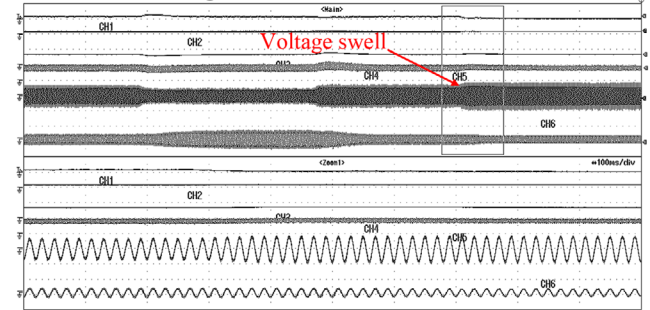
FIGURE 28 The effect of sudden change in three-phase ac load on PV system and grid as mentioned in test case-IV of section-3 (a) The effect of sudden increase of three-phase ac load on SSI based PV grid-tied system (b) The effect of sudden decrease of three-phase ac load on SSI based PV grid-tied system

CH1:PV Voltage= 100V/Div CH4:Dc-link current= 2A/Div
 CH2:PV Current= 10A/Div CH5:Grid voltage= 300V/Div
 CH3:Dc-link voltage= 600V/Div CH6:Grid Current= 5A/Div



(a) The effect of Voltage sag on SSI based PV grid-tied system

CH1:PV Voltage= 100V/Div CH4:Dc-link current= 2A/Div
 CH2:PV Current= 10A/Div CH5:Grid voltage= 300V/Div
 CH3:Dc-link voltage= 600V/Div CH6:Grid Current= 5A/Div



(b) The effect of Voltage swell on SSI based PV grid-tied system

FIGURE 29 The effect of grid disturbances on the SSI based PV grid-tied system (a) The effect of Voltage sag on SSI based PV grid-tied system (b) The effect of Voltage swell on SSI based PV grid-tied system

different solar radiations is presented in Figure 31 and is found to be approximately 94%. The spikes at time instants $t = 1, 2, 6$ s are due to the sudden change in the solar radiation. The comparative analysis of conventional [10] and proposed control schemes is presented in Table 3.

4 | CONCLUSION

A new single-stage SSI is used in this paper. The advantages of this topology are stabilized dc-link voltage, lesser voltage stress, minimal requirement of passive elements, similar switching state, switch count, and modulation schemes of VSI. A new peak power control is designed to track maximum power from the PV system and to generate a duty cycle for the inverter. A robust grid-oriented control is designed and investigated with five case studies. In all the cases, the optimal performance of the dc-link voltage controller and the current controller can be observed from the simulation and experimental results. The effects of load dynamics (dc and ac) and grid disturbances of the

TABLE 3 Comparative analysis of the conventional [10] and proposed control schemes

Performance index	Conventional [10]	Proposed
Peak overshoot (V)(variable irradiance)	50	30
Undershoot (V)(variable irradiance)	45	20
Peak overshoot (V)(voltage sag)	10	5
Undershoot (V)(voltage swell)	10	4
THD (%) (simulation)	2.4	1.48
THD (%) (Experimental)	>simulation [10]	2.93
MPPT block	No	Yes
Dc and ac load analysis	No	Yes
Transients analysis of PV system	No	Yes

grid-tied SSI on the PV system are thoroughly analyzed in this work. Especially, the reverse operation of SSI is analyzed by connecting a dc load across the dc-link capacitor. The future work can be focused on replacing the perturb and observe maximum

rPLL1:U1	49.866 Hz	Order	I1 [A]	hdf[%]	Order	I1 [A]	hdf[%]
Urms1	109.32 V	Total	2.8142		dc		
Irms1	2.8162 A	41	0.0049	0.174	42	0.0076	0.269
P1	306.24 W	43	0.0033	0.118	44	0.0050	0.178
S1	307.86 VA	45	0.0012	0.044	46	0.0032	0.112
Q1	-31.50 var	47	0.0017	0.061	48	0.0092	0.327
λ 1	0.9948	49	0.0037	0.133	50	0.0045	0.161
ϕ 1	05.87 °	51	0.0036	0.128	52	0.0037	0.131
Uthd1	2.763 %	53	0.0029	0.101	54	0.0088	0.312
Ithd1	2.933 %	55	0.0043	0.153	56	0.0078	0.278
Pthd1	0.004 %	57	0.0041	0.146	58	0.0064	0.229
Uthf1	1.561 %	59	0.0064	0.226	60	0.0039	0.138
Ithf1	2.520 %	61	0.0046	0.164	62	0.0027	0.096
Utif1	67.240	63	0.0059	0.211	64	0.0023	0.080
Itif1	116.282	65	0.0061	0.218	66	0.0034	0.120
hvf1	1.009 %	67	0.0058	0.207	68	0.0052	0.186
hcf1	1.086 %	69	0.0039	0.139	70	0.0068	0.241
Kfact1	1.8392	71	0.0025	0.088	72	0.0028	0.099
		73	0.0067	0.240	74	0.0050	0.177
		75	0.0042	0.149	76	0.0072	0.258
		77	0.0030	0.107	78	0.0075	0.267
		79	0.0036	0.130	80	0.0047	0.168

FIGURE 30 The real-time data for the THD analysis of the grid voltage and currents

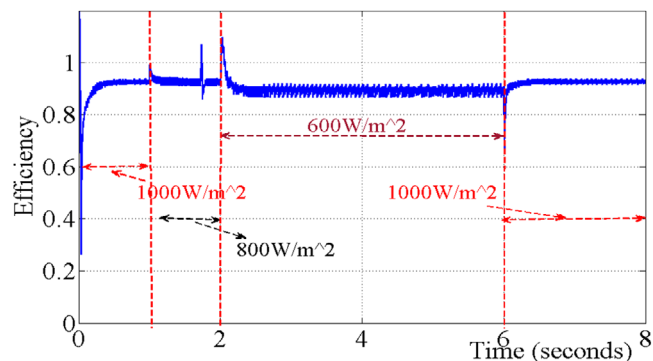


FIGURE 31 The efficiency of the entire system at variable irradiation conditions

power algorithm and PI based control system by an advanced power tracking controls and self-adaptive regulators to enhance the accuracy, efficiency, and reliability of the system.

ACKNOWLEDGMENTS

The authors wish to thank DST-SERB, statutory body established through an act of parliament: SERB Act 2008, Government of India for their financial assistance for the undergoing project under project reference no. SERB - SB/S3/EECE/090/2016 and also the management of NIT, Meghalaya (an institute of national importance) for their constant support to carry out the work.

ORCID

Hari Charan Nannam  <https://orcid.org/0000-0001-9266-1217>

REFERENCES

- Siwakoti, Y., et al.: Impedance-source networks for electric power conversion part i: A topological review. *IEEE Trans. Power Electron.* 30(2), 699–716 (2015)
- Zhang, L., et al.: A high step-up dc to dc converter under alternating phase shift control for fuel cell power system. *IEEE Trans. Power Electron.* 30(3), 1694–1703 (2015)
- Manoranjan S., Sivakumar, K.: A three-level LC-switching-based voltage boost NPC inverter. *IEEE Trans. Indus. Electron.* 64(4), 2876–2883 (2017)
- Peng, F.: Z-source inverter. *IEEE Trans. Indus. Appl.* 39(2), 504–510 (2003)
- Abdelhakim, A., Mattavelli, P., Spiazzi, G.: Three-phase split-source inverter (SSI): Analysis and modulation. *IEEE Trans. Power Electron.* 31(11), 7451–7461 (2016)
- Yang, S., et al.: Current-fed quasi-z-source inverter with voltage buck. *IEEE Trans. Ind. Appl.* 47(2), 882–892 (2011)
- Lee, S., et al.: Single-phase simplified split-source inverter (S^3I) for boost DC-AC power conversion. *IEEE Trans. Indus. Electron.* 66(10), 7643–7652 (2019)
- Lee, S., Heng, Y.: Improved single-phase split-source inverter with hybrid quasi-sinusoidal and constant PWM. *IEEE Trans. Indus. Electron.* 64(3), 2024–2031 (2017)
- Abdelhakim, A., Mattavelli, P., Spiazzi, G.: Three-phase three-level flying capacitors split source inverters: Analysis and modulation. *IEEE Trans. Indus. Electron.* 64(6), 4751–4580 (2017)
- Abdelhakim, A., et al.: Decoupled control scheme of grid-connected split-source inverters. *IEEE Trans. Ind. Electron.* 64(8), 6202–6211 (2017)
- Li, Y., et al.: Modeling and control of quasi-z-source inverter for distributed generation applications. *IEEE Trans. Ind. Electron.* 60(4), 1532–1541 (2013)
- Ho, A-V, Chun, T-W, Kim, H-G: Extended boost active-switched-capacitor/switched-inductor quasi-z-source inverters. *IEEE Trans. Power Electron.* 30(10), 5681–5690 (2015)
- Gajanayake, C., et al.: Extended-boost Z-source inverters. *IEEE Trans. Power. Electron.* 25(10), 2642–2652 (2010)
- Nguyen, M-K., Lim, Y-C., Cho, G-B: Switched-inductor quasi-z-source inverter. *IEEE Trans. Power Electron.* 26(11), 3183–3191 (2011)
- Lei, Q, Cao, D, Peng, FZ.: Novel loss and harmonic minimized vector modulation for a current-fed quasi-z-source inverter in HEV motor drive application. *IEEE Trans. Power. Electron.* 29(3), 1344–1357 (2014)
- Hassan, M., et al.: Three-phase split-source inverter-fed PV systems: Analysis and mitigation of common-mode voltage. *IEEE Trans. Power Electron.* 35(9), 9826–9840 (2020)
- Abdelhakim, A., Blaabjerg, F., Mattavelli, P.: Modulation schemes of the three-phase impedance source inverters-Part I: Classification and review. *IEEE Trans. Indus. Electron.* 65(8), 6309–6320 (2018)
- Abdelhakim, A., Blaabjerg, F., Mattavelli, P.: Modulation schemes of the three-phase impedance source inverters part II: Classification and review. *IEEE Trans. Indus. Electron.* 65(8), 6321–6332 (2018)
- Esrām, T., Chapman, P.: Comparison of photovoltaic array maximum power point tracking techniques. *IEEE Trans. Energy Convers.* 22(2), 439–449 (2007)
- Mohanty, S., Subudhi, B., Ray, P.: A grey wolf-assisted perturb and observe MPPT algorithm for a PV system. *IEEE Trans. Energy Convers.* 32(1), 340–347 (2017)
- Yin, B., et al.: An output power control strategy for a three phase PWM rectifier under unbalanced supply conditions. *IEEE Trans. Indus. Electron.* 55(5), 2140–2150 (2008)
- Etxeberria-Otadui, I., Viscarret, U., Caballero, M.: New optimized PWM VSC control structures and strategies under unbalanced voltage transients. *IEEE Trans. Indus. Electron.* 54(5), 2902–2914 (2007)
- Tang, C.-Y., et al.: Dc-link voltage control strategy for three-phase back-to-back active power conditioners. *IEEE Trans. Ind. Electron.* 62(10), 6306–6316 (2015)

24. Nannam, H., Babu, C., Banerjee, A.: Control and analysis of a 3-level diode clamped split source inverter in the applications of grid-tied photovoltaic systems. *Int. Trans. Electr. Energy Syst.* e12573 (2020). <https://doi.org/10.1002/2050-7038.12573>
25. Teodorescu, R., Liserre, M., Rodriguez, P.: *Grid converters for photovoltaic and wind power systems.* John Wiley & Sons, Ltd., (2011)
26. Umland, J., Safiuddin, M.: Magnitude and symmetric optimum criterion for the design of linear control systems: What is it and how does it compare with the others? *IEEE Trans. Ind. Appl.* 26(3), 489–497 (1990)
27. Blaabjerg, F., et al.: Overview of control and grid synchronization for distributed power generation systems. *IEEE Trans. Ind. Electron.* 53(5), 1398–1409 (2006)
28. Blasko, V., Kaura, V.: A new mathematical model and control of a three-phase ac-dc voltage source converter. *IEEE Trans. Power Electron.* 12(1), 116–123 (1997)
29. Yazdani, A., Iravani, R.: *Voltage-sourced converters in power systems: Modeling, control and applications.* John Wiley & Sons, Inc., (2010)
30. Nousiainen, L., et al.: Photovoltaic generator as an input source for power electronic converters. *IEEE Trans. Power Electron.* 28(6), 3028–3038 (2013)
31. Blagouchine, I.V., Moreau, E.: Analytic method for the computation of the total harmonic distortion by the cauchy method of residues. *IEEE Trans. Comm.* 59(9), 2478–2491 (2011)
32. IEEE recommended practice and requirements for harmonic control in electric power systems, IEEE Std 519- 2014 (Revision of IEEE Std 519-1992), 2014, pp. 1–29
33. Mahmoud, Y., Xiao, W., Zeineldin, H.: A simple approach to modeling and simulation of photovoltaic modules. *IEEE Trans. Sustainable Energy* 3(1), 185–186 (2012)
34. Villalva, M., Gazoli, J., Filho, E.: Comprehensive approach to modeling and simulation of photovoltaic arrays. *IEEE Trans. Power Electron.* 24(5), 1198–1208 (2009)
35. Mukund, R. Patel: *Wind and solar power systems: Design, analysis, and operation.* 2 Taylor and Francis group, 6000 Broken sound park way NW, Suite 300, Boca Raton. (2006)

How to cite this article: Nannam HC, Banerjee A, Guerrero JM. Analysis of an interleaved control scheme employed in split source inverter based grid-tied photovoltaic systems. *IET Renew Power Gener.* 2021;15:1301–1314.
<https://doi.org/10.1049/rpg2.12108>